

## Research Paper

## Compressional and shear wave velocities of Fe-bearing silicate post-perovskite in Earth's lowermost mantle

Jing Yang<sup>a,b,\*</sup>, Suyu Fu<sup>a,c</sup>, Jin Liu<sup>a,d</sup>, Jung-Fu Lin<sup>a</sup><sup>a</sup> Department of Earth and Planetary Sciences, Jackson School of Geosciences, University of Texas at Austin, Austin, TX 78712, USA<sup>b</sup> Earth and Planet Laboratory, Carnegie Science, Washington, DC 20015, USA<sup>c</sup> Department of Earth and Planetary Science, The University of Tokyo, Bunkyo, Tokyo 113-0033, Japan<sup>d</sup> School of Environmental and Chemical Engineering, Yanshan University, Qinhuangdao 066004, PR China

## ARTICLE INFO

## Article history:

Received 6 May 2024

Revised 19 July 2024

Accepted 14 August 2024

Available online 17 August 2024

## Keywords:

Fe-bearing post-perovskite

D" layer

Sound velocities

## ABSTRACT

The bridgmanite (Bgm) to silicate post-perovskite (PPv) phase transition is believed to be the main cause for the distinct seismic features observed in the D" layer, the lowermost region of the Earth's mantle. However, the transition depth and elasticity of the PPv phase have been highly debated, as the chemical complexity within the D" layer can largely affect the Bgm-PPv transition pressure and the associated velocity contrast. Experimental measurements of sound velocities for PPv with different chemical compositions under relevant lowermost-mantle conditions are essential but remain limited. In this study, we have reliably measured both compressional wave velocity ( $V_p$ ), shear wave velocity ( $V_s$ ), and density, for two Fe-bearing PPv compositions [(Mg<sub>0.85</sub>Fe<sub>0.15</sub>)SiO<sub>3</sub> and (Mg<sub>0.75</sub>Fe<sub>0.25</sub>)SiO<sub>3</sub>] at lowermost mantle pressures using Impulsive Stimulated Light Scattering (ISS), Brillouin Light Scattering (BLS), and X-ray Diffraction (XRD) in diamond anvil cells. Our results indicate that the velocities of Fe-bearing PPv at 120 GPa can be described by the following relationships:  $V_s$  (km/s) = 7.65–2.8 $X_{Fe}$  and  $V_p$  (km/s) = 14.11–3.8 $X_{Fe}$ , where  $X_{Fe}$  represents mole fraction of the Fe content. The variations in the Fe content of PPv may provide one of the explanations for the seismic lateral variations observed at the Earth's core mantle boundary. By comparing our results with the high-pressure velocities of Bgm, our velocity model suggests significant discontinuities across the Bgm-PPv transition, characterized by a reduction in both  $V_p$  and  $V_\phi$ , and an increase in  $V_s$ . These findings highlight the importance of considering the influence of chemical composition, particularly Fe content which could vary significantly at the D" region, on the seismic properties of the PPv phase. The observed velocity contrasts across the Bgm-PPv transition may contribute to the complex seismic signatures observed in the D" layer, underscoring the potential role of this phase transition in interpreting the seismic features of the lowermost mantle region.

© 2024 China University of Geosciences (Beijing) and Peking University. Published by Elsevier B.V. on behalf of China University of Geosciences (Beijing). This is an open access article under the CC BY-NC-ND license (<http://creativecommons.org/licenses/by-nc-nd/4.0/>).

## 1. Introduction

Seismic compressional wave ( $V_p$ ) and shear wave ( $V_s$ ) velocities of the Earth's lower mantle are observed to mostly increase monotonically with depth, with no noticeable seismic discontinuities, from 670 km to approximately 2600 km in depth. At approximately 100 – 450 km above the CMB (referred as D" layer), however, significant seismic discontinuities have been detected, with increased  $V_s$ ,  $V_s$  splitting anisotropy (Lay and Helmberger, 1983). These seismic features in the D" region seem to be distributed globally, although the magnitude and depth of these seismic anomalies vary significantly in different regions (Lay and

Helmberger, 1983; Zhang and Lay, 1984; Kendall and Nangini, 1996; Ding and Helmberger, 1997; Reasoner and Revenaugh, 1999; Lay et al., 2004; Thomas et al., 2004; Kito et al., 2007; Hutko et al., 2008; Chaloner et al., 2009; Schlaphorst et al., 2016), which is typically attributed to laterally distributed chemical heterogeneity, thermal perturbations in the D" region or solid-solid phase transition (Murakami et al., 2004; Grocholski et al., 2012; Cobden et al., 2015).

The origin of the D" discontinuity was first proposed to be associated with a solid-solid phase transition with a large positive Clapeyron slope. This hypothesis gained support with the discovery of the Bridgmanite (Bgm) to silicate post-perovskite (PPv) phase transition, which exhibits a Clapeyron slope of  $\sim 7$  MPa/K (Murakami et al., 2004; Oganov and Ono, 2004; Tsuchiya et al., 2004). Calculations further show that the Bgm-PPv transition pro-

\* Corresponding author.

E-mail address: [jyang@carnegiescience.edu](mailto:jyang@carnegiescience.edu) (J. Yang).

duces a positive  $V_S$  change ( $\Delta V_S$ ) up to 5%, while the change in  $V_P$  ( $\Delta V_P$ ) is significantly less at  $\sim 1\%$  (Iitaka et al., 2004; Oganov and Ono, 2004; Caracas and Cohen, 2005; Wookey et al., 2005; Tsuchiya and Tsuchiya, 2006; Wentzcovitch et al., 2006). In addition, theoretical studies have indicated that PPv can display strong lattice preferred orientations and, together with its high predicted elastic anisotropy, can produce 1%–3%  $V_S$  splitting anisotropy with  $V_{SH} > V_{SV}$  (Iitaka et al., 2004), which explain the seismic observed shear wave splitting (Wu et al., 2017). However, the direct velocity measurements across the Bgm-PPv transition in order to probe the discontinuity and anisotropy at core mantle boundary (CMB) condition have never been done due to the experimental challenge and technique limitation. Thus, the interpretation of the aforementioned seismic features at the D'' region using the occurrence of PPv phase has remained mostly theoretical.

D'' layer also show chemical complexity based on previous results (Garnero et al., 2016). It has been proposed that D'' layer is chemically heterogeneous in Fe content in different lowermost mantle regions. For example, the enrichment of Fe in the D'' region can be caused by the chemical interaction between the lowermost mantle and the outer core (Knittle and Jeanloz, 1989; Otsuka and Karato, 2012). On the other hand, the subducted materials with mid-ocean ridge basalt (MORB) may penetrate into the depth of CMB, modifying the Fe content in the host minerals of the D'' region by stirring and by chemical reactions with material from the surrounding lowermost mantle (Dobson and Brodholt, 2005). Fe has been observed to affect the depth and width of the Bgm to PPv transition, which can in turn provide important insight for the phase assemblages and Fe concentrations near the CMB in these different regions. For example, previous studies show that the pressure range for the PPv transition in a pyrolitic composition is about  $\sim 10 - 30$  GPa, broader than the transition range of  $3 - 15$  GPa for a mid-ocean-ridge-basalt (MORB) composition (Grocholski et al., 2012), which is with implication for the detectability of seismic discontinuities in global scale. In addition, PPv with 40 mol.% Fe (Mao et al., 2006), as well other Fe enriched candidate [eg. Ferropericlae (Wicks et al., 2010), and hydrogen-bearing  $\text{FeO}_2$  (Liu et al., 2017)] may explain the seismic features of ultra-low-velocity zones (ULVZs), which are  $5 - 40$  km thick regions with large reductions of  $V_P$  and  $V_S$  in D'' region. Therefore, to study the Fe effects on the sound velocity and density of PPv phase are of great interest as it can provide crucial constraints on the magnitude of seismic heterogeneities in different regions.

Various studies have extensively investigated the thermoelastic properties of the PPv over a wide range of Fe content. Equation of state of Fe-bearing PPv has been studied to understand the Fe effect on the density and bulk modulus of these phases at lowermost mantle conditions (Mao et al., 2005; Catalli et al., 2010). It has been shown that addition of Fe can greatly increase the density of PPv, but has a negligible effect on the isothermal modulus ( $K_T$ ) and bulk sound velocity ( $V_\phi$ ) if the amount of Fe is less than 10 mol.% (Shieh et al., 2006; Guignot et al., 2007). Since the compression data for PPv containing greater than 10% of Fe is still limited, the Fe effect on the  $K_T$  over higher Fe content remain controversial.

Sound velocity measurements of PPv with different Fe contents has been attempted by different techniques, including Brillouin Light scattering (BLS) and resonant inelastic X-ray scattering (NRIXS). BLS is only capable to measure  $V_S$  of the transparent or semi-transparent samples at above 40 GPa since the  $V_P$  of the samples is masked by the diamond  $V_S$  signals. As such, only  $V_S$  of Fe-free polycrystalline PPv has been measured up to 172 GPa. Comparing with the measured  $V_S$  of Fe-free Bgm, it showed a velocity contrast of  $\sim 0.5\%$  (Murakami et al., 2007), which suggest that the PPv transition may not explain the  $V_S$  discontinuity at D'' layer. NRIXS allows determination of the phonon density of state (DOS)

of samples containing  $^{57}\text{Fe}$  isotope, which can determine the Debye sound velocity ( $V_D$ ) that related to  $V_P$  and  $V_S$  from the low-energy portion of the phonon DOS. Together with  $V_\phi$  from X-ray diffraction measurements,  $V_P$  and  $V_S$  can be calculated respectively. The  $V_P$  and  $V_S$  of PPv with 40% of Fe determined from NRIXS can reconcile the seismic observations of ULVZs. However, it has been recently suggested that the sound velocities of Fe-bearing PPv and Bgm can be underestimated, which were lower than the expected values due to the presence of abnormal phonon mode contribution in the low-energy spectrum of the partial phonon density of states (McCammon et al., 2016).

Directly measured  $V_P$  and  $V_S$  of PPv with varying Fe contents are still lacking but can provide valuable experimental constraints on the elastic properties and seismic observations. In this work, we have used complimentary laser and X-ray spectroscopic techniques coupled with a DAC to measure  $V_P$  using ISS,  $V_S$  using BLS, and density using XRD of Fe-bearing PPv at D'' pressures. We aim to investigate the Fe effects on the  $V_P$ ,  $V_S$  and  $V_\phi$  of PPv phase and evaluate velocity discontinuities, correlations as well as Poisson's ratio across the Bgm-PPv transition at lowermost mantle pressures.

## 2. Methods

Fe-bearing silicate post-perovskite samples (PPv15 or PPv25) were synthesized from starting materials of silicate glass [ $(\text{Mg}_{0.85}\text{Fe}_{0.15})\text{SiO}_3$ ] and polycrystalline enstatite [ $(\text{Mg}_{0.75}\text{Fe}_{0.25})\text{SiO}_3$ ], respectively. The starting glass was synthesized from a mixture of  $\text{MgO}$ ,  $\text{Fe}_2\text{O}_3$ , and  $\text{SiO}_2$  powders in appropriate ratios using a high-temperature furnace (See (Mao et al. 2014) for more details on the synthesis of Fe-bearing silicate glass). Enstatite was synthesized from the powders of  $\text{SiO}_2$ ,  $\text{MgO}$ , and  $\text{Fe}_2\text{O}_3$  mixed in the appropriate ratio, which was placed in a furnace with well controlled oxygen fugacity (Mao et al., 2010). An electron microprobe was used to analyze the chemical composition and homogeneities of the starting glass and enstatite, which showed  $(\text{Mg}_{0.85}\text{Fe}_{0.15})\text{SiO}_3$  for the glass and  $(\text{Mg}_{0.75}\text{Fe}_{0.25})\text{SiO}_3$  for enstatite sample, respectively.

The glass starting materials were polished down to approximately  $10 - 12$   $\mu\text{m}$  in thickness and subsequently cut into pieces around  $60$   $\mu\text{m}$  in diameter, while polycrystalline enstatite was slightly compressed between two diamond anvils to prepare for a sample disk of  $10$   $\mu\text{m}$  in thickness and  $60$   $\mu\text{m}$  in diameter. The sample disk was loaded into a sample chamber and sandwiched between two dried NaCl layers of approximately  $5$   $\mu\text{m}$  in thickness which was served as the pressure medium, pressure calibrant, and thermal insulator. Each sample assemblage was loaded into a short symmetric diamond anvil cell (DAC) equipped with a pair of beveled diamonds of  $150/300$   $\mu\text{m}$  in culet size and a pre-indented Re gasket with a hole  $80$   $\mu\text{m}$  in diameter and  $28$ - $\mu\text{m}$  thick. The diamond anvils were selected for ultralow birefringence using polarized petrographic microscope to allow success of the ISS experiments. Enstatite loaded in the sample chamber was directly compressed to  $125$  GPa at  $300$  K, and laser heated at  $\sim 2000$  K for approximately  $5$  h while the glass sample was compressed to  $143$  GPa at  $300$  K and laser heated at  $\sim 2200$  K for approximately  $30$  h to fully transform the starting materials to PPv at GSECARS of the Advanced Photon Source (APS), Argonne National Laboratory (ANL). During the synthesis, the laser heating spot (approximately  $10$   $\mu\text{m}$ ) was constantly scanned across the whole sample by slowly moving the sample stage every few seconds. This process was used to minimize chemical diffusion and to ensure that the sample was heated as uniformly as possible. Analysis of the XRD spectra of the laser heated samples using an incident X-ray beam of  $2$   $\mu\text{m}$  and a wavelength of  $0.3344$   $\text{\AA}$  confirmed the successful synthesis of the

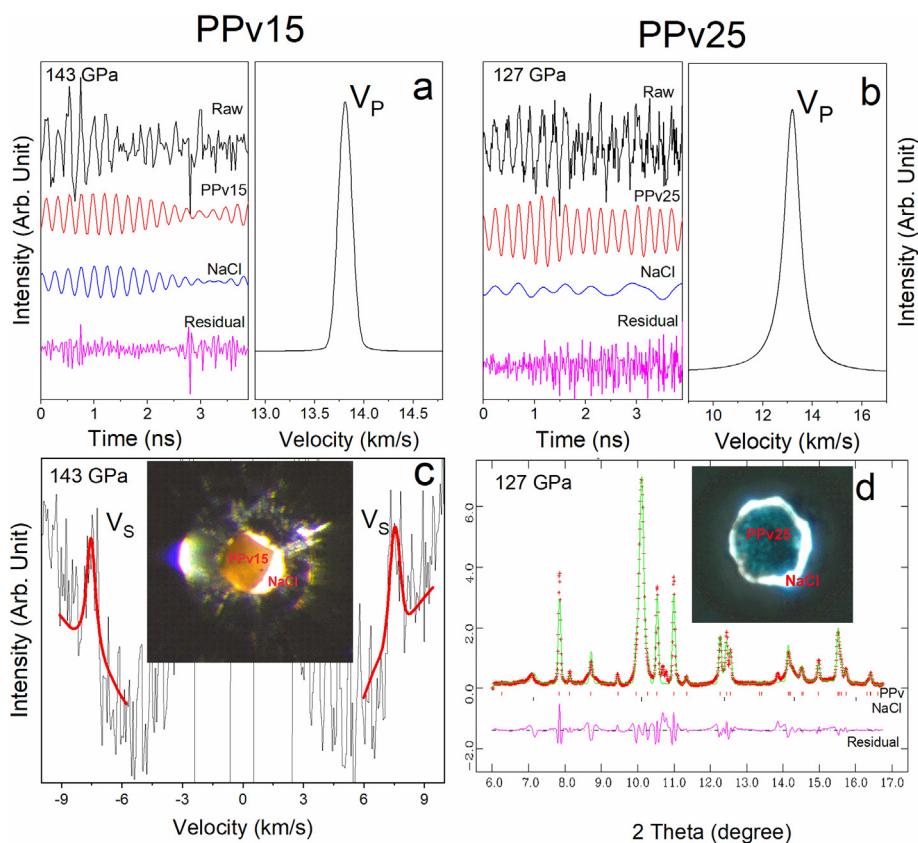


**Fig. 1.** Representative experimental spectra of the synthesized Fe-bearing PPv samples at high pressures and 300 K. Impulsive light scattering spectrum (left panel) and Fourier-transformed power spectrum for compressional wave velocity ( $V_P$ ) (right panel) of PPv15 at 143 GPa (a) and PPv25 at 127 GPa (b); (c) Brillouin spectrum of PPv15 at 143 GPa, together with an inset photo of the sample with NaCl as pressure medium; (d) Raw X-ray diffraction spectrum of PPv25 with a photo insert of the sample and NaCl. Black lines in Fig. 1c represent the raw Brillouin spectrum and red lines show the fitted shear wave velocity ( $V_S$ ). Red crosses in Fig. 1d indicate the raw diffraction spectrum while the green lines represent Le Bail fit; red and black vertical bars indicate peaks for PPv25 and NaCl phases, respectively. Incident X-ray wavelength was 0.3344 Å.

PPv15 and PPv25 samples (Fig. 1d and Supplementary data Fig. S1). XRD spectra measured from various spots of the samples showed consistent lattice parameters within experimental uncertainties, indicating that the starting samples were successfully transformed into PPv phase. The pressure of the sample was determined from analysis of the XRD spectra using the NaCl EoS (Fei et al., 2007). After a pressure change, each sample was then laser annealed at around 1800 K for 2 h across the whole sample at 13IDD beamline of the GSECARS to release possible non-hydrostaticity and to further confirm the crystallinity of PPv samples as well as the sample pressures. In total, XRD patterns were collected from PPv15 at 143, 134 and 122 GPa and from PPv25 at 127, 122 GPa. XRD patterns of the PPv samples have been measured in decompression at each given pressure to determine the lattice parameters, unit cell volume and density of the samples. The cell parameters of PPv15 and PPv25 were calculated using the Le Bail fits to the experimental XRD patterns. Densities of the samples were then calculated using the starting composition of the samples and the derived unit cell volumes.

The synthesized PPv15 and PPv25 samples were used for BLS and ISS experiments in the Mineral Physics Laboratory of the University of Texas at Austin. BLS and ISS spectra were collected from PPv15 in the transmitted geometry, but PPv25 sample was only sufficiently transparent for ISS measurements (it was too dark to permit BLS measurements). The BLS system was equipped with a Coherent Verdi V2 laser operating at 532 nm wavelength, together with a JRS interferometer and an APD detector (Count-10B Photo Counting Module with approximately 5 cps from Laser Components, Inc.). The laser power was set at 0.6 W for most of

the measurements. The focused laser beam size at the sample position was approximately 20  $\mu\text{m}$  in diameter while the scattering angle of the BLS system was set at 47°, which was calibrated against SiO<sub>2</sub> glass and purified water standards. The data collection time was typically 12 – 18 h for each pressure point due to relatively weak acoustic signals from the samples when compared with the background noise and strong diamond  $V_S$  peak. To reduce the overlap of the diamond  $V_S$  peak with the sample  $V_S$  peak, the crystallographic orientations for each pair of diamond anvils (the anvils were standard cut design in 100 orientation) used in the experiments were aligned in the alignment process of the DAC. BLS spectra of the samples were collected from an orientation where the  $V_S$  of the diamond anvils were at maximum velocity to allow the maximum window and lowest background for collecting the  $V_S$  peak of the samples. The measured BLS spectra were fitted with a Lorentzian peak shape (Fig. 1c).

High-pressure ISS spectra were collected from both PPv15 and PPv25 samples. The ISS system was equipped with a pump laser of 1064 nm wavelength and a probe laser with a 532-nm wavelength (Talisker, Coherent Company), which had a pulse width of 15 ps. The pump laser was split into two beams which were then recombined at the sample position with a crossing angle of 20.3° and a focused beam size of 25  $\mu\text{m}$ . The probe laser was delayed by an Aerotech linear stage by as long as 20 ns, while the diffracted ISS signals were collected by a photodiode detector. The data collection time for each ISS spectrum was typically 4 h with 1–2 mm step size. The time-domain raw ISS spectra were Fourier-transformed to frequency-domain power spectra based on the Burg method using the MATLAB and OriginPro 9.1 software. The

acoustic wave velocities of the sample were calculated from the frequency based on the laser-beam geometry (Fig. 1a), which was calibrated using glass and water standards. The interfacial waves in the ISS spectra were extracted in some data analyses but were not used for the modelled velocity profiles. Thus, only  $V_p$  velocities of the samples were used from the ISS measurements while the  $V_s$  velocities were derived from the BLS experiments.

In order to confirm the chemical homogeneity and grain size of the Fe-bearing samples after laser heating as well as after BLS and ISS measurements, we conducted chemical analysis and collected backscattered electron images of the quenched samples using electron microprobe. The grain size of PPv15 is less than 1  $\mu\text{m}$  and for PPv25 is less than 3  $\mu\text{m}$  as shown in the Backscatter Electron images (Supplementary data Fig. S4). We further did wavelength-dispersive spectrometry analysis for the quenched PPv15 and PPv25 samples coated with Ir. Multiple spots were randomly selected on the sample to determine the chemical compositions. It showed that the Fe contents in quenched PPv15 sample was 13.1%–13.5% mol.%, while in PPv25, the Fe contents ranges from 25.1 mol.% – 27.8 mol.% (Supplementary data Table S2), indicating that the chemical heterogeneity related velocity differences within the sample could be negligible. We should also note that the measured velocity was an averaged velocity from hundreds of grains with randomly distributed orientation. The incident laser beam size of the BLS and ISS measurements on the samples with 1 – 3  $\mu\text{m}$  grain size are about 30 – 40  $\mu\text{m}$ , thus the measured velocity which would be from  $\sim$  500 grains polycrystalline PPv with 15  $\mu\text{m}$  thickness was comparable to aggregate sound velocity with no preferred orientation.

### 3. Results

The formation of the Fe-bearing polycrystalline PPv phase for PPv15 and PPv25 was confirmed using *in situ* XRD measurements. Rietveld whole-profile refinement using GSAS provide densities of the samples at high pressures (Fig. 1d, Supplementary data Fig. S1 and Table 1). At 122 GPa and 300 K, the densities of PPv15 and PPv25 are 5.794 g/cm<sup>3</sup> and 5.884 g/cm<sup>3</sup> respectively, which are consistent with previous studies (Dorfman and Duffy, 2014). No observable preferred orientations were found in formed PPv phases based on the XRD patterns (Fig. 1d and Supplementary data Fig. S1) as the measured relative peak intensities agree well with

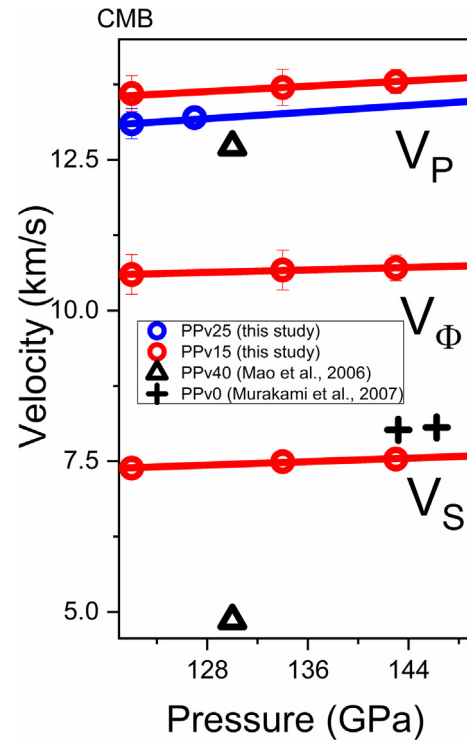


Fig. 2. Velocity profiles of Fe-bearing PPv and Bgm at lowermost mantle pressures. Red symbols represent measured velocity for PPv15, while blue symbols are for PPv25. The measured velocity results were linearly fitted to show their pressure gradients as shown in red lines for PPv15 and blue line for  $V_p$  of PPv25. For PPv15,  $V_p$  results are measured from ISS experiments,  $V_s$  from BLS experiments, and  $V_\phi$  results are calculated using  $V_\phi = \sqrt{V_p^2 - 4V_s^2/3}$ . Triangles represent the  $V_p$  and  $V_s$  data for PPv with 40% of Fe (PPv40) (Mao et al. 2006) and plus symbols represent the  $V_s$  for Fe-free PPv (PPv0) (Murakami et al., 2007).

that expected from a powder diffraction pattern. The synthesized PPv15 was optically translucent in transmitted light (Fig. 1c inset) to sufficiently permit both ISS and BLS measurements at 143, 134 and 122 GPa, while PPv25 was sufficiently semi-translucent (Fig. 1d inset) to only allow for ISS measurements at 127 and 122 GPa (Figs. 1, 2; Table 1). The different optical properties for PPv15 and PPv25 is due to the different Fe concentrations

Table 1  
Experimentally measured sound velocities of PPv with different Fe contents at high pressures.

Mg <sub>0.85</sub> Fe <sub>0.15</sub> SiO <sub>3</sub> (PPv15) This study				
Pressure (GPa)	$V_p$ (km/s)	$V_s$ (km/s)	$V_\phi$ (km/s)	density(g/cm <sup>3</sup> )
143	13.8(2)	7.54(8)	10.7(3)	6.152
134	13.7(3)	7.44(9)	10.7(4)	6.021
122	13.6(3)	7.38(9)	10.6(4)	5.794
Mg <sub>0.75</sub> Fe <sub>0.25</sub> SiO <sub>3</sub> (PPv25) This study				
Pressure (GPa)	$V_p$ (km/s)	$V_s$ (km/s)	$V_\phi$ (km/s)	density(g/cm <sup>3</sup> )
127	13.2(1)			5.913
122	13.1(2)			5.884
Mg <sub>0.6</sub> Fe <sub>0.4</sub> SiO <sub>3</sub> (PPv40) (Mao et al., 2006)				
Pressure (GPa)	$V_p$ (km/s)	$V_s$ (km/s)	$V_\phi$ (km/s)	density(g/cm <sup>3</sup> )
130	12.72	4.86	11.43	6.08
MgSiO <sub>3</sub> (PPv0) (Murakami et al., 2007)				
Pressure (GPa)	$V_p$ (km/s)	$V_s$ (km/s)	$V_\phi$ (km/s)	density(g/cm <sup>3</sup> )
143		8.02		
146		8.06		
159		8.12		
172		8.30		

and grain sizes. The  $Fe^{2+}/Fe^{3+}$  ratio were not analyzed, which may also contribute to the different colors in the in the PPv15 and PPv25.

Sound velocities of PPv15 and PPv25 as a function of pressure were plotted in Fig. 2. These results allow us to evaluate the pressure gradients at 300 K for both  $V_p$  and  $V_s$ . Within the investigated pressure range, the  $V_p$  and  $V_s$  values as a function of pressure for PPv15 and PPv25 are linearly fitted to evaluate the velocity gradient at lowermost mantle pressures with a starting pressure chosen at 120 GPa, which yields Eqs (1)–(3):

$$V_s^{PPv15} = 7.37(\text{km/s}) + 0.007 \times P(\text{GPa}) \quad (1)$$

$$V_p^{PPv15} = 13.55(\text{km/s}) + 0.011 \times P(\text{GPa}) \quad (2)$$

$$V_p^{PPv25} = 13.07(\text{km/s}) + 0.014 \times P(\text{GPa}) \quad (3)$$

Comparison of the velocity of PPv15 and PPv25 at 120 GPa shows that  $V_p$  PPv15 is 0.48 km/s (or 3.5%) lower than that of PPv25 as a result of additional 10 mol.% Fe substitution (Fig. 2). Together with the  $V_p$  and  $V_s$  measurements from ISS and BLS, the bulk sound velocity ( $V_\phi$ ) of PPv15 is calculated using  $V_\phi = \sqrt{V_p^2 - 4V_s^2/3}$  (Fig. 2). For comparison, Fig. 2 incorporates velocity measurements for Fe-free PPv (PPv0) and PPv with 40% of Fe (PPv40), obtained from the studies conducted by Murakami et al. (2007) and Mao et al. (2006), respectively. The set of data demonstrate that incorporating Fe in PPv exhibits a negative effect on both of the  $V_s$  and  $V_p$  across the pressure range investigated.

To better illustrate the Fe effect on the velocities of the PPv, we plotted the relationship between sound velocities and Fe content in Fig. 3. Despite the limited experimental data available on the sound velocities for Fe-free PPv, PPv15, PPv 25 and PPv40, the data presented indicate that addition of Fe in PPv produces a linear decrease in  $V_p$  and linear increase in and  $V_\phi$  respectively. However, the relationship between  $V_s$  and Fe content shows a non-linear behavior, deviating from the typical linear trends observed for other elastic properties (eg. Density,  $V_p$ ,  $V_s$ ,  $V_\phi$  and  $C_{ij}$ ) in PPv and other lower mantle minerals (Jacobsen et al., 2002; Mao et al., 2005). The non-linear relationship between  $V_s$  and Fe content may provide the supporting evidence that the  $V_s$  value for PPv40, determined from NRIXS measurements, is underestimated. Thus, assuming a linear relationship with increasing Fe content and also considering pressure effect, we got the results at given 120 GPa as Eqs. (4)–(6):

$$V_s = 7.65(\text{km/s}) - 2.8 \times X_{Fe} \quad (4)$$

$$V_p = 14.11(\text{km/s}) - 3.8 \times X_{Fe} \quad (5)$$

$$V_\phi = 10.10(\text{km/s}) + 3.2 \times X_{Fe} \quad (6)$$

where the  $X_{Fe}$  is the molar fraction of the Fe content in the PPv phase. Based on the fitted data, we found that the  $V_s$  for PPv40, as determined from NRIXS was underestimated by more than 25%.

To apply our results to understand seismic features at the lowermost mantle regions, we have also calculated Poisson's ratio ( $\nu$ ) of Fe-bearing Bgm and PPv as Eq. (7):

$$\nu = \frac{1}{2} \frac{(V_p/V_s)^2 - 2}{(V_p/V_s)^2 - 1} \quad (7)$$

Based on the calculations using measured  $V_p$  and  $V_s$ , Poisson's ratio of PPv15 is 0.29 at  $\sim 270$  km above the CMB and its pressure gradient is  $-1.19 \times 10^{-5} \text{ km}^{-1}$ , a slightly negative value at lowermost mantle pressures (Fig. 4).

## 4. Discussion

### 4.1. Velocity contrast across the Bgm and PPv the phase transition

To evaluate the velocity contrast across the Fe-bearing Bgm and PPv phase boundary, we have modelled velocity profiles of the Fe-bearing Bgm and PPv at high pressure. The following procedure has been used to model the equation of state (EoS), compressional wave velocity ( $V_p$ ) and shear wave velocity ( $V_s$ ) of Fe-bearing Bgm at lowermost-mantle pressures. Third-order Eulerian finite-strain Eqs. (8)–(10) were used to calculate the adiabatic bulk modulus  $K_S$  and shear modulus  $G$  at high pressure using reported adiabatic bulk and shear moduli at ambient conditions ( $K_{S0}$  and  $G_0$ ) (Li and Zhang, 2005; Chantel et al., 2012):

$$K_S = K_{S0}(1 + 2f)^{5/2} \{1 + [3K'_S - 5]f\} \quad (8)$$

$$G = (1 + 2f)^{5/2} \{G_0 + [3G'K_{S0} - 5G_0]f\} \quad (9)$$

$$f = \left(\frac{1}{2}\right) \left[ \left(\frac{\rho}{\rho_0}\right)^{2/3} - 1 \right] \quad (10)$$

where  $K'_S$  is the pressure derivative of the adiabatic bulk modulus,  $G'$  is the pressure derivative of the shear modulus,  $f$  is the Eulerian finite strain, and  $\rho_0$  and  $\rho$  are density of the sample at ambient conditions and high pressure, respectively. The aggregate  $V_p$  and  $V_s$  can be calculated using the following Eqs. (11)–(12) at each given pressure or density:

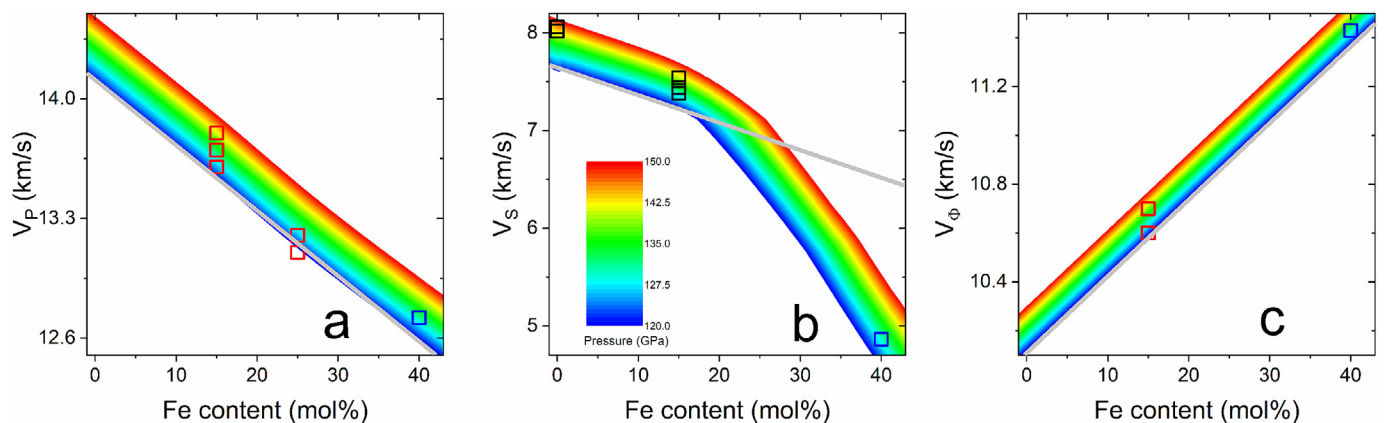
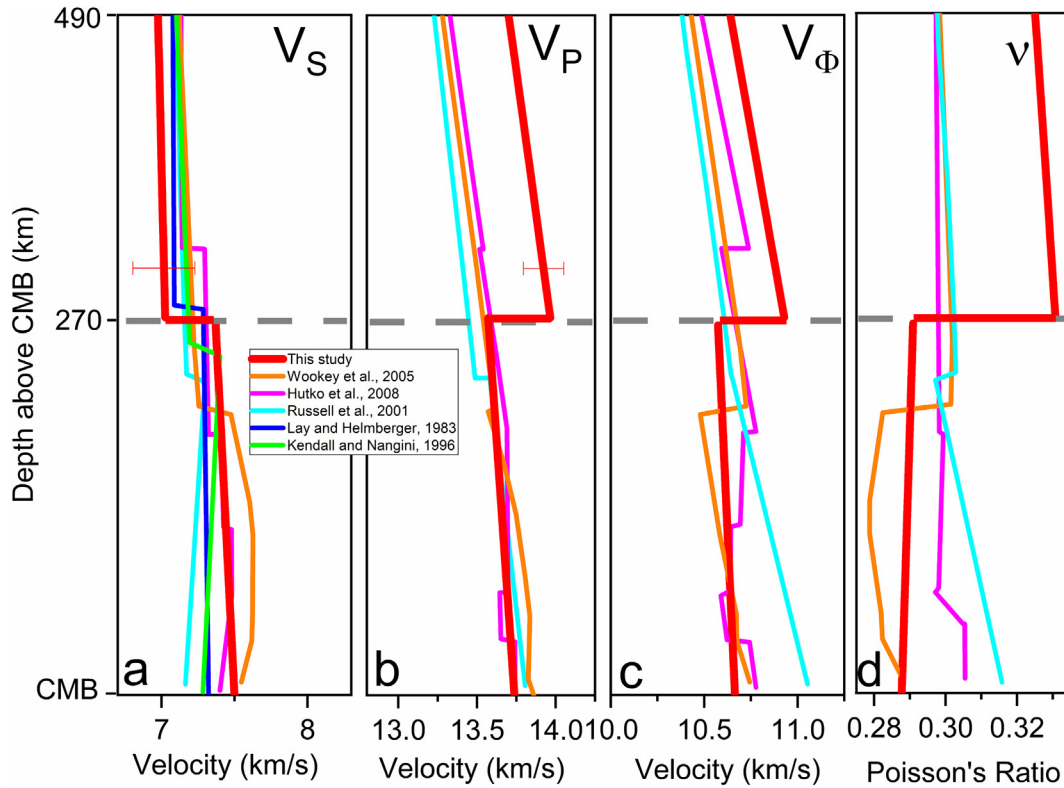


Fig. 3. Velocities of Fe-free and Fe-bearing PPv as a function of Fe concentration plotted in pressure contours. Red symbols represent PPv15 and PPv25 in this study; black symbols represent Fe-free PPv [Murakami et al., 2007]; blue represent PPv containing 40 mol% Fe (Mao et al., 2006). Pressure contouring level is from 120 to 150 GPa with layer boundaries. The grey lines show the linear approximation of sound velocity changes with Fe content at 120 GPa.



**Fig. 4.** Velocity profiles and Poisson's ratio across the Fe-bearing PPv transition at the D'' region. Representative seismic observations of the D'' region are also plotted for comparison (blue, pink, green and cyan lines) (Lay and HelMBERGER, 1983; Kendall and Nangini, 1996; Russell et al., 2001; Hutko et al., 2008). The transition depth is selected to be at 2620 km depth or 270 km above the core-mantle boundary (grey dotted line). Thick red lines represent modeled velocity profiles and Poisson's ratio ( $\nu$ ) of PPv and Bgm containing 15% Fe at high pressure and 300 K. Orange lines are theoretical data for velocity profile across the phase boundary between Bgm and PPv (Wookey et al., 2005).

$$V_p = \sqrt{(4K_s/3 + G)G/\rho} \quad (11)$$

$$V_s = \sqrt{G/\rho} \quad (12)$$

Here high-pressure density of Bgm was calculated using the third-order Birch-Murnaghan EoS and previously reported EoS parameters obtained in previous X-ray diffraction measurements (Ballaran et al., 2012; Chantel et al., 2012) (Eq. 13) (Supplementary data Table S1):

$$P = 3K_{T0} \left[ (\rho/\rho_0)^{7/3} - (\rho/\rho_0)^{5/3} \right] \left\{ 1 + 3/4(K'_T - 4) \left[ (\rho/\rho_0)^{2/3} - 1 \right] \right\} \quad (13)$$

where  $K_{T0}$  is the isothermal bulk modulus at ambient conditions,  $K'_T$  is the pressure derivative of the isothermal bulk modulus, and  $\rho_0$  is the density at ambient conditions. For the Fe-bearing Bgm, datasets for the aforementioned elasticity parameters (Chantel et al., 2012) are limited to the bridgmanite with  $\text{MgSiO}_3$  pure end-member and ( $\text{Mg}_{0.95}\text{Fe}_{0.05}\text{SiO}_3$ ) with 5% Fe. Although elastic parameters of Bgm with 10% Fe and 10% Al are also available in a recent Brillouin study (Kurnosov et al., 2017), the extrapolation of this set of data show significant velocity differences especially in  $V_s$  when compared with that reported in Chantel et al. (2012) above 30 GPa (Supplementary data Fig. S2). The differences may be due to the presence of  $\text{Fe}^{3+}$  and/or  $\text{Al}^{3+}$ . Thus, this set of data for Fe,Al-bearing bridgmanite was not employed in any extrapolations in this study as our study here focuses on sound velocity profiles of Fe-bearing Bgm and PPv.

To test the validity of the extrapolation from literature data for Bgm5, we have measured  $V_p$  up to 68 GPa and  $V_s$  up to 88 GPa for

polycrystalline Bgm5 using ISS and BLS (Supplementary data Fig. S2). It showed that the measured velocities are in great agreement of with the extrapolated data for Bgm5 (Supplementary data Fig. S2). We have used a linear extrapolation for the Fe substitution effects on the EoS and elastic parameters to obtain velocity profiles ( $V_p$  and  $V_s$ ) for Bgm15 and Bgm25 up to 120 GPa as Eqs. (13)–(14):

$$dV_{p,s}/dX_{Fe} = [V_{p,s}(\text{bgm5}) - V_{p,s}(\text{bgm0})]/5 \quad (13)$$

$$V_{p,s}(P) = V_{p,s}(\text{km/s}) - dV_{p,s}/dX_{Fe} \times X_{Fe} \quad (14)$$

where  $X_{Fe}$  is the amount of Fe content in mol percent in the sample and  $dV/dX_{Fe}$  is the compositional gradient of the given velocity. Uncertainties in these calculations are obtained through standard error propagations. The calculated compositional gradient of velocity  $dV_p/dX_{Fe}$  and  $dV_s/dX_{Fe}$  are  $\sim -0.046$  and  $-0.016$  at ambient conditions, respectively, and are  $-0.039$  and  $-0.038$  at 120 GPa for Bgm. The estimated velocity differences between Bgm and PPv depend on the choice of the input thermoelastic parameters of Bgm for the modelling. Although input data are rather limited, several iterations were performed based on the datasets reported (Supplementary data Table S1). All of the data used for the modelling consistently show an increased  $V_s$  and decreased  $V_p$  across the PPv phase transition when the velocity profiles of Bgm and PPv are compared at 120 GPa. With the extrapolated data, we plotted the Bgm15 and PPv15 velocities as a function of density as shown in Supplementary data Fig. S3. A decrease in both  $V_p$  and  $V_\Phi$  and an increase in  $V_s$  are observed as the density increases.

## 4.2. Geophysical implications

Numerous seismic studies have reported the presence of the seismic discontinuity in the D'' region, located approximately 200 – 300 km above the core-mantle boundary (CMB). Lay and Helmberger (1983) detected a  $2.75\% \pm 0.25\%$  increase in  $V_S$  approximately 280 km above the CMB using direct S and ScS waveform analysis (Lay and Helmberger, 1983). Kendall and Nangini (1996) reported clear evidence for a 2.45%–2.75% increase in  $V_S$  at 250 km above the CMB beneath the Caribbean (Kendall and Nangini, 1996). Russell et al. (2001) observed a localized discontinuous increase in both  $V_P$  (0.75%) and  $V_S$  (1.7%) at 230 km above the CMB beneath the central Pacific region (Russell et al., 2001). Later, Hutko et al. (2008) reported a small decrease of  $-0.007\% \pm 0.15\%$  in  $V_P$  accompanied by a  $1.5\% \pm 0.5\%$  increase in  $V_S$  at 299 – 324 km above the CMB under the Cocos plate. Notably, the bulk sound velocity ( $V_\phi$ ) decreased by  $-1.0\% \pm 0.5\%$  at this depth (Hutko et al., 2008).

A number of possible explanations for the D'' seismic features has been proposed, including the thermochemical heterogeneities, plastic flow induced fabric within the D'' layer and a phase transition from Bgm to PPv. Cobden et al. (2012) compared mantle models with and without the inclusion of post-perovskite and found that models incorporating a PPv-bearing core-mantle boundary (CMB) region provide a significantly better fit to global and regional seismic data compared to PPv-free models (Cobden et al., 2012). Cobden and Thomas (2013) analyzed P- and S-wave reflections in the D'' region and proposed that in regions such as the Caribbean, characterized by high-amplitude, negative polarity P waveforms and positive polarity S waveforms, the phase transition from Bgm to PPv is the most likely explanation for the observed discontinuity (Cobden and Thomas, 2013). Ab initio calculations by Wookey et al. (2005) suggest that the phase transition from Bgm to PPv has different effects on seismic velocities, with  $V_S$  increasing by around 4% at the discontinuity, while the  $V_\phi$  is strongly reduced (Wookey et al., 2005). This anticorrelation results in an almost negligible  $V_P$  discontinuity. These studies collectively provide evidence for a seismic discontinuity in the D'' region, likely associated with the phase transition from Bgm to PPv, exhibiting distinct signatures in seismic wave velocities, particularly the velocity increase in  $V_S$ , and the anticorrelation between  $V_S$  and  $V_\phi$  anomalies.

The direct measurement of  $V_P$  and  $V_S$  sound velocities of the PPv under relevant pressure conditions in this study, in conjunction with measured and modeled sound velocities of Bgm, enables us to assess the velocity contrast across the transition at a given depth and evaluate the likelihood of the presence of the PPv phase. In Fig. 4, we have plotted the velocity contrast between Bgm and PPv with 15% Fe content on top of seismic observations and ab initio calculations. Our data suggest a  $\sim 5.3\%$  increase in  $V_S$ , a  $\sim 2.8\%$  decrease in  $V_P$ , and a  $\sim 3.5\%$  decrease in  $V_\phi$ . The anti-correlation between  $V_S$  and  $V_\phi$  is consistent with seismic observations. It is noteworthy that the measurements were conducted at room temperature, and high temperatures may have a negative effect on the velocities, potentially reducing the measured velocity contrast across the phase transition. Several studies have claimed that there may be a region of coexistence phases of Bgm and PPv in the D'' layer, and the layer of two-phase coexistence may be too thick for the Bgm-PPv phase transition to be the sole cause of the observed seismic discontinuities (Kuwayama et al., 2022). However, Langrand et al. (2019) suggested that the transformation kinetics of the Bgm to PPv transition could affect the reflection coefficients of  $V_P$  and  $V_S$  by more than an order of magnitude (Langrand et al., 2019). Consequently, thick layer of coexisting Bridgmanite and post-perovskite can be detected using seismic reflections. On the other hand, theoretical studies by

Wentzcovitch et al. (2023) proposed that the presence of  $\text{Fe}^{3+}$ ,  $\text{Fe}^{2+}$ , and  $\text{Al}^{3+}$  may play a role in the transition pressure and sharpness of the D'' discontinuity associated with the Bgm to PPv transition (Wentzcovitch et al., 2023). Further investigations on the velocity measurements of PPv compositions with varying  $\text{Fe}^{3+}$  and  $\text{Al}^{3+}$  concentrations will help resolve this hypothesis.

Previous seismic tomographic studies commonly show evidence for a laterally-varying  $V_S$  discontinuity in some localized lowermost mantle (Kendall and Nangini, 1996; Lay et al., 2004). Also, in the global scale, the seismic discontinuities are commonly observed in faster-than-average-velocity regions that may be related to the cold subducted slabs (Cobden et al., 2015). These laterally seismic variations can be attributed to either chemical heterogeneity or preferred crystal orientation aligned with flow direction in the PPv phase (Asplet et al., 2020). Although no preferred orientation has been observed in our experiment, the sound velocities of PPv at lowermost lower mantle are more sensitive to Fe content compared to the pressure effect over the experimental pressure range. Thus, it may suggest that the chemical composition of the PPv would be the dominant factor to affect the sound velocities at lowermost pressure range if PPv presents there. The variations of seismic velocities at base of lower mantle may be a reflection of variation in Fe concentration in different regions. These Fe distribution heterogeneity can be caused by either localized reactions between silicate mantle and liquid outer core (Otsuka and Karato, 2012) or the penetration of Fe enriched slab materials such banded iron formation (Dobson and Brodholt, 2005). On the other hand, our results show that the variation in  $V_S$  ( $\frac{\partial \ln V_S}{\partial X_{\text{Fe}}} = -0.39$ ) that varies with up to 40 mol.% Fe content is larger than that variation in  $V_P$  ( $\frac{\partial \ln V_P}{\partial X_{\text{Fe}}} = -0.28$ ) at 120 GPa, which suggests that  $V_S$  is more sensitive to Fe content than that of  $V_P$ . This could be the potential reason that seismic  $V_S$  discontinuities at the D'' layer are more prevalent than  $V_P$  discontinuities if Fe concentration dominate the sound velocity of PPv. Our one-dimensional velocity model shows a substantial reduction of 12% in the Poisson's ratio, decreasing from approximately 0.33 to 0.29, across the Bgm to PPv phase transition (Fig. 4). In seismic studies where both P wave and S wave arrivals are detected, the Poisson's ratio can be directly determined. However, in most of the seismic tomography studies, the correlation between  $V_P$  and  $V_S$  is robust up to 1500 km but gradually deteriorates towards the bottom of the mantle. Consequently, the variation in Poisson's ratio in the lowermost mantle remain ambiguous, with estimates ranging from a positive change of  $\sim 6\%$  to a negative change of around  $-5\%$  (Weber, 1993). The observed variations in the Poisson's ratio across the Earth's lower mantle can be used to infer the thermal or chemical perturbations (Saltzer et al., 2004). We propose that the phase transition could be a potential explanation for the variations in the Poisson's ratio that observed in the lowermost mantle. The significant reduction in the Poisson's ratio associated with this phase transition may contribute to the observed seismic signatures and provide insights into the mineralogical and compositional heterogeneities present in D'' layer.

## 5. Conclusion

We have directly measured sound velocities of two PPv compositions, PPv15 and PPv25 to provide mineral physical constraints on the velocity profiles across the Fe-bearing Bgm-PPv phase transition. The occurrence of the Fe-bearing Bgm-PPv transition exhibit a significant increase in  $V_S$  accompanied by a reduction in both  $V_P$  and  $V_\phi$  which is consistent with the first-order seismic observation in the Earth's lowermost mantle region. Our study also shows a substantial effect of Fe on the sound velocities of PPv phase, highlighting the importance of considering the influence of chemical

compositions, particularly Fe content, on the seismic signatures of Earth's lowermost mantle. Future studies on the seismic profiles of Fe-Al-bearing PPv with co-existing bridgmanite and ferropericlase at elevated pressure-temperature conditions, together with information about their two-phase textures and single-crystal elasticity, are critically needed to decipher detailed seismic features and realistic dynamic flow patterns at the lowermost mantle.

### CRedit authorship contribution statement

**Jing Yang:** Writing – original draft, Methodology, Formal analysis, Data curation. **Suyu Fu:** Writing – review & editing, Methodology. **Jin Liu:** Writing – review & editing, Methodology. **Jung-Fu Lin:** Writing – review & editing, Writing – original draft, Methodology, Funding acquisition, Conceptualization.

### Declaration of Competing Interest

The authors declare that they have no known competing financial interests or personal relationships that could have appeared to influence the work reported in this paper.

### Acknowledgments

We acknowledge H.C. Watson for providing the glass and enstatite starting materials, V. Prakapenka for experimental assistance with the synthesis of the PPv samples and XRD experiments. We appreciate E. Garnero and S. P. Grand for constructive discussions. J.F. Lin acknowledges supports from the U.S. National Science Foundation Geophysics Program (EAR-2001381). We acknowledge GSECARS of the APS for use of the diffraction and laser heating facilities. This research utilized the resources of the Advanced Photon Source, a U.S. Department of Energy (DOE) Office of Science User Facility operated for the DOE Office of Science by Argonne National Laboratory under Contract No. DE-AC02-06CH11357. Data used in this study are available upon request to Jing Yang (jyang@carnegiescience.edu) and Jung-Fu Lin (afu@jsg.utexas.edu).

### Appendix A. Supplementary data

Supplementary data to this article can be found online at <https://doi.org/10.1016/j.gsf.2024.101915>.

### References

Asplet, J., Wookey, J., Kendall, M., 2020. A potential post-perovskite province in D'' beneath the Eastern Pacific: evidence from new analysis of discrepant SKS-SKKS shear-wave splitting. *Geophys. J. Int.* 221 (3), 2075–2090.

Ballaran, T.B., Kurnosov, A., Glazyrin, K., Frost, D.J., Merlini, M., Hanfland, M., Caracas, R., 2012. Effect of chemistry on the compressibility of silicate perovskite in the lower mantle. *Earth Planet. Sci. Lett.* 333, 181–190.

Caracas, R., Cohen, R., 2005. Effect of chemistry on the stability and elasticity of the perovskite and post-perovskite phases in the MgSiO<sub>3</sub>-FeSiO<sub>3</sub>-Al<sub>2</sub>O<sub>3</sub> system and implications for the lowermost mantle. *Geophys. Res. Lett.* 32 (16), L16310.

Catalli, K., Shim, S.-H., Prakapenka, V., Zhao, J., Sturhahn, W., 2010. X-ray diffraction and Mössbauer spectroscopy of Fe<sup>3+</sup>-bearing Mg-silicate post-perovskite at 128–138 GPa. *Am. Mineral.* 95 (2–3), 418–421.

Chaloner, J.W., Thomas, C., Rietbrock, A., 2009. P- and S-wave reflectors in D'' beneath southeast Asia. *Geophys. J. Int.* 179 (2), 1080–1092.

Chantel, J., Frost, D.J., McCammon, C.A., Jing, Z., Wang, Y., 2012. Acoustic velocities of pure and iron-bearing magnesium silicate perovskite measured to 25 GPa and 1200 K. *Geophys. Res. Lett.* 39, L19307.

Cobden, L., Mosca, I., Trampert, J., Ritsema, J., 2012. On the likelihood of post-perovskite near the core-mantle boundary: A statistical interpretation of seismic observations. *Phys. Earth Planet. Interiors* 210, 21–35.

Cobden, L., Thomas, C., 2013. The origin of D'' reflections: A systematic study of seismic array data sets. *Geophys. J. Int.* 194 (2), 1091–1118.

Cobden, L., Thomas, C., Trampert, J., 2015. Seismic detection of post-perovskite inside the Earth. *The Earth's Heterogeneous Mantle: A Geophysical, Geodynamical, and Geochemical Perspective*, 391–440.

Ding, X., Helmberger, D.V., 1997. Modelling D'' structure beneath Central America with broadband seismic data. *Phys. Earth Planet. Interiors* 101 (3), 245–270.

Dobson, D.P., Brodholt, J.P., 2005. Subducted banded iron formations as a source of ultralow-velocity zones at the core-mantle boundary. *Nature* 434 (7031), 371–374.

Dorfman, S., Duffy, T., 2014. Effect of Fe-enrichment on seismic properties of perovskite and post-perovskite in the deep lower mantle. *Geophys. J. Int.* 197 (2), 910–919.

Fei, Y., Ricolleau, A., Frank, M., Mibe, K., Shen, G., Prakapenka, V., 2007. Toward an internally consistent pressure scale. *Proceedings of the National Academy of Sciences* 104(22), 9182–9186.

Garnero, E.J., McNamara, A.K., Shim, S.-H., 2016. Continent-sized anomalous zones with low seismic velocity at the base of Earth's mantle. *Nature Geosci.* 9 (7), 481–489.

Grocholski, B., Catalli, K., Shim, S.-H., Prakapenka, V., 2012. Mineralogical effects on the detectability of the postperovskite boundary. *Proceedings of the National Academy of Sciences* 109(7), 2275–2279.

Guignot, N., Andraut, D., Morard, G., Bolfan-Casanova, N., Mezouar, M., 2007. Thermoelastic properties of post-perovskite phase MgSiO<sub>3</sub> determined experimentally at core-mantle boundary P-T conditions. *Earth Planet. Sci. Lett.* 256 (1–2), 162–168.

Hutko, A.R., Lay, T., Revenaugh, J., Garnero, E.J., 2008. Anticorrelated Seismic Velocity Anomalies from Post-Perovskite in the Lowermost Mantle. *Science* 320, 1070–1074.

Iitaka, T., Hirose, K., Kawamura, K., Murakami, M., 2004. The elasticity of the MgSiO<sub>3</sub> post-perovskite phase in the Earth's lowermost mantle. *Nature* 430 (6998), 442–445.

Jacobsen, S.D., Reichmann, H.J., Spetzler, H.A., Mackwell, S.J., Smyth, J.R., Angel, R.J., McCammon, C.A., 2002. Structure and elasticity of single-crystal (Mg, Fe) O and a new method of generating shear waves for gigahertz ultrasonic interferometry. *J. Geophys. Res. Solid Earth* 107, B2037.

Kendall, J., Nangini, C., 1996. Lateral variations in D'' below the Caribbean. *Geophys. Res. Lett.* 23 (4), 399–402.

Kendall, J.M., Nangini, C., 1996. Lateral variations in D'' below the Caribbean. *Geophys. Res. Lett.* 23 (4), 399–402.

Kito, T., Rost, S., Thomas, C., Garnero, E.J., 2007. New insights into the P- and S-wave velocity structure of the D'' discontinuity beneath the Cocos plate. *Geophys. J. Int.* 169 (2), 631–645.

Knittle, E., Jeanloz, R., 1989. Simulating the core-mantle boundary: An experimental study of high-pressure reactions between silicates and liquid iron. *Geophys. Res. Lett.* 16 (7), 609–612.

Kurnosov, A., Marquardt, H., Frost, D., Ballaran, T.B., Ziberna, L., 2017. Evidence for a Fe<sup>3+</sup>-rich pyrolytic lower mantle from (Al, Fe)-bearing bridgmanite elasticity data. *Nature* 543 (7646), 543.

Kuwayama, Y., Hirose, K., Cobden, L., Kusakabe, M., Tateno, S., Ohishi, Y., 2022. Post-perovskite phase transition in the pyrolytic lowermost mantle: Implications for ubiquitous occurrence of post-perovskite above CMB. *Geophys. Res. Lett.* 49 (1).

Langrand, C., Andraut, D., Durand, S., Konôpková, Z., Hilairet, N., Thomas, C., Merkel, S., 2019. Kinetics and detectability of the bridgmanite to post-perovskite transformation in the Earth's D'' layer. *Nature Commun.* 10 (1), 5680.

Lay, T., Garnero, E., Russell, S., 2004. Lateral variation of the D'' discontinuity beneath the Cocos Plate. *Geophys. Res. Lett.* 31, L15612.

Lay, T., Helmberger, D.V., 1983. A lower mantle S-wave triplication and the shear velocity structure of D''. *Geophys. J. Int.* 75 (3), 799–837.

Li, B., Zhang, J., 2005. Pressure and temperature dependence of elastic wave velocity of MgSiO<sub>3</sub> perovskite and the composition of the lower mantle. *Phys. Earth Planet. Interiors* 151 (1–2), 143–154.

Liu, J., Hu, Q., Kim, D.Y., Wu, Z., Wang, W., Xiao, Y., Chow, P., Meng, Y., Prakapenka, V. B., Mao, H.-K., 2017. Hydrogen-bearing iron peroxide and the origin of ultralow-velocity zones. *Nature* 551 (7681), 494.

Mao, Z., Lin, J., Jacobs, C., Watson, H., Xiao, Y., Chow, P., Alp, E., Prakapenka, V., 2010. Electronic spin and valence states of Fe in CaIrO<sub>3</sub>-type silicate post-perovskite in the Earth's lowermost mantle. *Geophys. Res. Lett.* 37, L22304.

Mao, Z., Lin, J.-F., Yang, J., Wu, J., Watson, H.C., Xiao, Y., Chow, P., Zhao, J., 2014. Spin and valence states of iron in Al-bearing silicate glass at high pressures studied by synchrotron Mössbauer and X-ray emission spectroscopy. *Am. Mineral.* 99 (2–3), 415–423.

Mao, W.L., Meng, Y., Shen, G., Prakapenka, V.B., Campbell, A.J., Heinz, D.L., Shu, J., Caracas, R., Cohen, R.E., Fei, Y., 2005. Iron-rich silicates in the Earth's D'' layer. *Proceedings of the National Academy of Sciences of the United States of America* 102 (28), 9751–9753.

Mao, W.L., Mao, H.-K., Sturhahn, W., Zhao, J., Prakapenka, V.B., Meng, Y., Shu, J., Fei, Y., Hemley, R.J., 2006. Iron-rich post-perovskite and the origin of ultralow-velocity zones. *Science* 312 (5773), 564–565.

McCammon, C., Caracas, R., Glazyrin, K., Potapkin, V., Kantor, A., Sinmyo, R., Prescher, C., Kuppenko, I., Chumakov, A., Dubrovinsky, L., 2016. Sound velocities of bridgmanite from density of states determined by nuclear inelastic scattering and first-principles calculations. *Progress in Earth and Planetary Science* 3 (1), 10.

Murakami, M., Hirose, K., Kawamura, K., Sata, N., Ohishi, Y., 2004. Post-perovskite phase transition in MgSiO<sub>3</sub>. *Science* 304 (5672), 855–858.

Murakami, M., Sinogeikin, S.V., Bass, J.D., Sata, N., Ohishi, Y., Hirose, K., 2007. Sound velocity of MgSiO<sub>3</sub> post-perovskite phase: A constraint on the D'' discontinuity. *Earth Planet. Sci. Lett.* 259 (1–2), 18–23.

Murakami, M., Sinogeikin, S.V., Bass, J.D., Sata, N., Ohishi, Y., Hirose, K., 2007. Sound velocity of MgSiO<sub>3</sub> post-perovskite phase: A constraint on the D'' discontinuity. *Earth Planet. Sci. Lett.* 259 (1), 18–23.

- Oganov, A.R., Ono, S., 2004. Theoretical and experimental evidence for a post-perovskite phase of  $\text{MgSiO}_3$  in Earth's D'' layer. *Nature* 430 (6998), 445–448.
- Otsuka, K., Karato, S.-I., 2012. Deep penetration of molten iron into the mantle caused by a morphological instability. *Nature* 492 (7428), 243–246.
- Reasoner, C., Revenaugh, J., 1999. Short-period P wave constraints on D'' reflectivity. *J. Geophys. Res. Solid Earth* 104 (B1), 955–961.
- Russell, S.A., Reasoner, C., Lay, T., Revenaugh, J., 2001. Coexisting shear-and compressional-wave seismic velocity discontinuities beneath the central Pacific. *Geophys. Res. Lett.* 28 (11), 2281–2284.
- Saltzer, R.L., Stutzmann, E., van der Hilst, R.D., 2004. Poisson's ratio in the lower mantle beneath Alaska: Evidence for compositional heterogeneity. *J. Geophys. Res. Solid Earth* 109, B06301.
- Schlaphorst, D., Thomas, C., Holme, R., Abreu, R., 2016. Investigation of core–mantle boundary topography and lowermost mantle with P4KP waves. *Geophysical Journal International* 204 (2), 1060–1071.
- Shieh, S.R., Duffy, T.S., Kubo, A., Shen, G., Prakapenka, V.B., Sata, N., Hirose, K., Ohishi, Y., 2006. Equation of state of the postperovskite phase synthesized from a natural (Mg, Fe)  $\text{SiO}_3$  orthopyroxene. *Proceedings of the National Academy of Sciences of the United States of America* 103 (9), 3039–3043.
- Thomas, C., Garnero, E.J., Lay, T., 2004. High-resolution imaging of lowermost mantle structure under the Cocos plate. *J. Geophys. Res. Solid Earth* 109, B08307.
- Tsuchiya, T., Tsuchiya, J., 2006. Effect of impurity on the elasticity of perovskite and postperovskite: Velocity contrast across the postperovskite transition in (Mg, Fe, Al)(Si, Al) $\text{O}_3$ . *Geophys. Res. Lett.* 33 (12), L12S04.
- Tsuchiya, T., Tsuchiya, J., Umemoto, K., Wentzcovitch, R.M., 2004. Phase transition in  $\text{MgSiO}_3$  perovskite in the earth's lower mantle. *Earth Planet. Sci. Lett.* 224 (3–4), 241–248.
- Weber, M., 1993. P-and S-wave reflections from anomalies in the lowermost mantle. *Geophys. J. Int.* 115 (1), 183–210.
- Wentzcovitch, R.M., Tsuchiya, T., Tsuchiya, J., 2006.  $\text{MgSiO}_3$  postperovskite at D'' conditions. *Proceedings of the National Academy of Sciences of the United States of America* 103 (3), 543–546.
- Wentzcovitch, R.M., Valencia-Cardona, J.J., Zhuang, J., Shukla, G., Sarkar, K., 2023. The Post-Perovskite Transition in Fe-and Al-Bearing Bridgmanite: Effects on Seismic Observables. *J. Geophys. Res. Solid Earth* 128 (3), e2022JB025475.
- Wicks, J.K., Jackson, J.M., Sturhahn, W., 2010. Very low sound velocities in iron-rich (Mg, Fe)O: Implications for the core–mantle boundary region. *Geophys. Res. Lett.* p. 37.
- Wookey, J., Stackhouse, S., Kendall, J.-M., Brodholt, J., Price, G.D., 2005. Efficacy of the post-perovskite phase as an explanation for lowermost-mantle seismic properties. *Nature* 438 (7070), 1004–1007.
- Wu, X., Lin, J.-F., Kaercher, P., Mao, Z., Liu, J., Wenk, H.-R., Prakapenka, V.B., 2017. Seismic anisotropy of the D'' layer induced by (001) deformation of post-perovskite. *Nat. Commun.* 8, 14669. <https://doi.org/10.1038/ncomms14669>.
- Zhang, J., Lay, T., 1984. Investigation of a lower mantle shear wave triplication using a broadband array. *Geophys. Res. Lett.* 11 (6), 620–623.